



1 Slow build-up of turbidity currents triggered by a moderate 2 earthquake in the Sea of Marmara

3

4 Pierre Henry¹, M Sinan Özeren², Nurettin Yakupoğlu³, Ziyadin Çakir³, Emmanuel de
5 Saint-Léger⁴, Olivier Desprez de Gésincourt⁴, Anders Tengberg⁵, Cristele Chevalier⁶,
6 Christos Papoutsellis¹, Nazmi Postacioğlu⁷, Uğur Dogan⁸, Hayrullah Karabulut⁹,
7 Gülsen Uçarkuş³, M Namık Çağatay³

8

9 ¹Aix Marseille Univ, CNRS, IRD, INRAE, Coll France, CEREGE, Aix-en-Provence,
10 France, ²Istanbul Technical University, Eurasia Institute of Earth Sciences, Maslak,
11 Istanbul, Turkey, ³Istanbul Technical University, Geological Engineering Dept.,
12 Maslak, Istanbul, Turkey, ⁴CNRS, DT INSU, Parc national d'instrumentation
13 océanographique, Plouzané, France, ⁵Aanderaa Data Instruments AS, Bergen,
14 Norway, ⁶Aix Marseille Univ, CNRS, IRD, MIO, Aix-en-Provence, France, ⁷Istanbul
15 Technical University, Physics Dept., Maslak, Istanbul, Turkey, ⁸Yıldız Technical
16 University, Geomatic Engineering Dept., Istanbul, Turkey, ⁹Bogazici University,
17 KOERI, Istanbul, Turkey

18

19 *Correspondence to:* Pierre Henry (henry@cerege.fr)

20

21 **Abstract.** Earthquake-induced submarine slope destabilization is known to cause
22 debris flows and turbidity currents, but the hydrodynamic processes associated with
23 these events remain poorly understood. Records are scarce and this notably limits
24 our ability to interpret marine paleoseismological sedimentary records. An
25 instrumented frame comprising a pressure recorder and a Doppler recording current
26 meter deployed at the seafloor in the Sea of Marmara Central Basin recorded
27 consequences of a $M_w = 5.8$ earthquake occurring Sept 26, 2019 and of a $M_w = 4.7$
28 foreshock two days before. The smaller event caused sediment resuspension but no
29 strong current. The larger event triggered a complex response involving a mud flow
30 and turbidity currents with variable velocities and orientations, which may result from
31 multiple slope failures. A long delay of 10 hours is observed between the earthquake
32 and the passing of the strongest turbidity current. The distance travelled by the
33 sediment particles during the event is estimated to several kilometres, which could



34 account for a local deposit on a sediment fan at the outlet of a canyon, but not for the
35 covering of the whole basin floor. We show that after a moderate earthquake,
36 delayed turbidity current initiation may occur, possibly by ignition of a cloud of
37 resuspended sediment. Some caution is thus required when tying seismoturbidites
38 with earthquakes of historical importance. However, the horizontal extent of the
39 deposits should remain indicative of the size of the earthquake.

40 1. Introduction

41 Triggering of mass flows and turbidity currents by earthquakes is a hazard that
42 can damage infrastructure at the seafloor (Heezen et al., 1954) and may enhance co-
43 seismic tsunami generation (Okal and Synolakis, 2001; Synolakis et al., 2002; Hebert
44 et al., 2005; Ozeren et al., 2010). It is often considered that a peak ground acceleration
45 (PGA) of the order of 0.1 g is needed for an earthquake to trigger a submarine slope
46 instability (Dan et al., 2008; Nakajima and Kanai, 2000). However, a global compilation
47 of cable breaks shows that, exceptionally, mass flow have been triggered by individual
48 earthquakes of M_w as low as 3.1 (with $PGA \approx 10^{-3}$ g) and that, on the other hand many
49 $M_w > 7$ have failed to break cables, notably in zones (e.g. Japan Trench) where
50 sediment input is relatively low and earthquakes frequent (Pope et al., 2016). In the
51 Mediterranean region, the threshold is reportedly around $M_w = 5$.

52 In spite of this high regional variability, turbidite deposits in several seismically
53 active zones have been used successfully as paleoseismological event markers
54 (Goldfinger et al., 2003, 2012; McHugh et al., 2014; Ikehara et al., 2016). This requires
55 distinguishing between seismoturbidites, caused by earthquakes and related mass
56 wasting events, from those resulting from other processes (e.g. floods, storms,
57 sediment loading). Seismoturbidites are generally described as turbidite-homogenites
58 where a basal silt-sand bearing layer is overlaid by a layer of apparently homogenous
59 mud with small or gradual, if any, variations in grain size and chemical composition
60 (Polonia et al., 2013; McHugh et al., 2011; Çağatay et al. 2012; Eriş et al., 2012;
61 Gutierrez-Pastor et al., 2013; Beck et al., 2007). In lakes and closed basins several
62 characteristics of deposits following earthquake or landslides, such as the sharp
63 boundary between turbidite and homogenite layers, the alternation of silt/sand and
64 mud laminae within a single turbidite-homogenite unit and presence of bi-directional
65 cross- or flaser- bedding have been interpreted as indicators of deposition from
66 oscillatory currents associated with seiches or turbidity current reflection (Beck et al.,

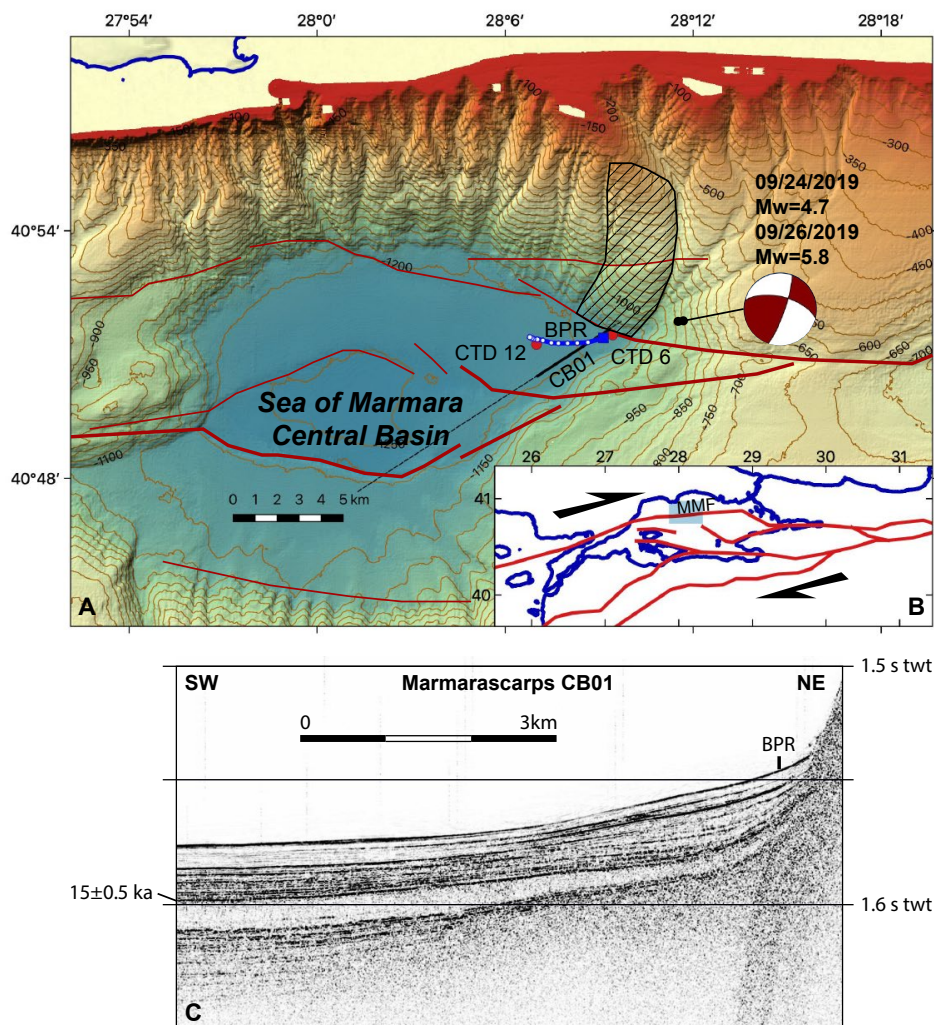


67 2007; Çağatay et al. 2012; McHugh et al., 2011). Seismoturbidites on ocean margins
68 have fairly similar characteristics to those in closed basins but their layering has been
69 interpreted differently, as a consequence of confluence (stacked or amalgamated
70 turbidites) or current speed variations (multi-pulsed turbidites) (Gutierrez-Pastor et al.,
71 2013; Nakajima and Kanai, 2000; Goldfinger et al., 2003). There is currently a lack of
72 in situ records that could substantiate inferred hydrodynamic processes. Monitoring
73 experiments brought records of representative cases of turbidity currents flowing in
74 submarine canyons and initiated by meteorological events and occasionally by
75 landslides (Azpiroz-Zabala et al., 2017; Khripounoff et al., 2012; Xu et al., 2004, 2010;
76 Liu et al., 2012; Hughes Clarke, 2016). Oscillatory currents resulting from internal
77 waves have been recorded after landslides in lakes (Brizuela et al., 2019). On the other
78 hand, most information on earthquake-triggered events is still indirect based on cable
79 ruptures (e.g. Pope, 2017; Hsu et al., 2008), combined with geomorphological and
80 sedimentological observations (Cattaneo et al., 2012; Piper et al., 1999), and
81 information from displaced instruments (Garfield et al., 1994). In Japan, in situ records
82 of pressure and temperature were obtained from displaced OBSs after the Tohoku
83 2011 M_w 9.1 earthquake (Arai et al., 2013), and from cabled observatories after the
84 Tokachi-Oki 2003 M_w 8.3 earthquake (Mikada et al., 2006) and after a moderate (M
85 5.4) earthquake off Izu Peninsula (Kasaya et al., 2009). After the large events, strong
86 currents of more than 1 m/s were implied starting 2-3 hours after the earthquake with
87 no indication of oscillation or pulsing. In the off-Izu case a mudflow was observed with
88 a camera 5 minutes after the earthquake and followed 15 minutes later by a change in
89 current direction and speed.

90 We here present results from an instrumental deployment at the seafloor that
91 accidentally recorded the consequences of earthquakes that occurred 09/24/2019 and
92 09/26/2019 in the Sea of Marmara with respective magnitudes 4.7 and 5.8 (Figure 1A).
93 Holocene seismoturbidite records in the Sea of Marmara basins display a recurrence
94 of 200 to 300 years, that roughly corresponds to the recurrence interval of $M_w > 7$
95 earthquakes (McHugh et al., 2006, 2014; Drab et al., 2012, 2015; Yakupoğlu et al.,
96 2018; Bulut et al., 2019). The pressure, temperature and current record from this single
97 instrument demonstrate that this moderate earthquake triggered turbidity currents.
98 However, the instrument suffered a rather complex sequence of disturbances and a
99 10 hours delay is observed between the earthquake and the recording of peak current.



100 We here propose a scenario which could explain the observations and discuss their
101 implications for the understanding of seismoturbidite records.



102
103 **Figure 1.** Context of instrumental deployment. (A) bathymetric map of the Sea of
104 Marmara Central Basin with simplified fault geometry (in red). The hatched zone is a
105 suspected mass wasting zone (Zitter et al., 2012). Location of instrumented frame
106 comprising bottom pressure recorder (BPR) and doppler current meter is indicated by
107 blue square. The blue banana with white dots represents the calculated trajectory of
108 a sedimentary particle during the waning phase of the turbidity current. Red dots are
109 CTD profiles 6 and 12 shown in supplementary material S1. Epicenter location of



110 earthquakes and the focal mechanism of the main shock are indicated. **(B)** Location
111 of study area. North Anatolian Fault system is shown in red. MMF is the Main
112 Marmara Fault. **(C)** Sediment sounder profile from Marmarascarps cruise (Armijo and
113 Malavieille, 2002). Indicative age of reflector from Beck et al. (2007). The instrument
114 (BPR) was deployed on a depositional fan at the base of slope and canyon outlet that
115 differ in character from the hemipelagite / turbidite-homogenite sequence in the
116 basin.

117 2. Context and data collection

118 A series of instrumental deployments was planned to record naturally occurring
119 resonant water column oscillations (seiches) at various locations in the Sea of
120 Marmara with the aim to improve tsunami models (Henry et al., 2021). An instrumented
121 frame was thus deployed at 40.8568° N, 28.1523° E and 1184 m water depth in the
122 Central Basin on May 9, 2019 and recovered 6 months later (11/19/2019) (Figure 1A).
123 This site is located at the outlet of a branched canyon system originating from the edge
124 of the continental shelf (Figure 1). Sediment sounder profiles indicate a depositional
125 fan or lobe is present at this location (Figure 1C). The short canyons observed on the
126 relatively steep sedimented slope ($\approx 10^\circ$) of the Sea of Marmara deep basins are
127 presumably fed by instabilities of the canyon heads and walls (Zitter et al. 2012;
128 Çağatay et al., 2015). In addition, the slope west of the canyons immediately north of
129 the deployment site hosts a mass wasting feature covering about 24 km² (Zitter et al.
130 2012). The Main Marmara Fault (MMF, Figure 1B), is defined as the part of the northern
131 branch of the North Anatolian Fault system crossing the Sea of Marmara (Le Pichon
132 et al., 2001, 2003). A splay of the MMF runs along the base of this slope (Armijo et al.,
133 2002; Grall et al., 2012; Sengor et al., 2014). The 09/24/2019 and 09/26/2019
134 earthquakes occurred beneath the canyon system and their epicenters are located 5
135 km ENE of the instrument, less than 500 m apart (Figure 1). The rupture occurred within
136 the crust at 9-13 km depth on a northward dipping fault located north of principal
137 displacement zone of the Main Marmara Fault. The focal mechanism and aftershock
138 distribution indicate right-lateral strike-slip with a reverse component (Karabulut et al.,
139 2021). The rupture did not reach the seafloor, nor caused a tsunami. For instance, tidal
140 gauge records obtained at Marmara Ereğlisi do not deviate more than 1hPa from a
141 fitted tidal model.

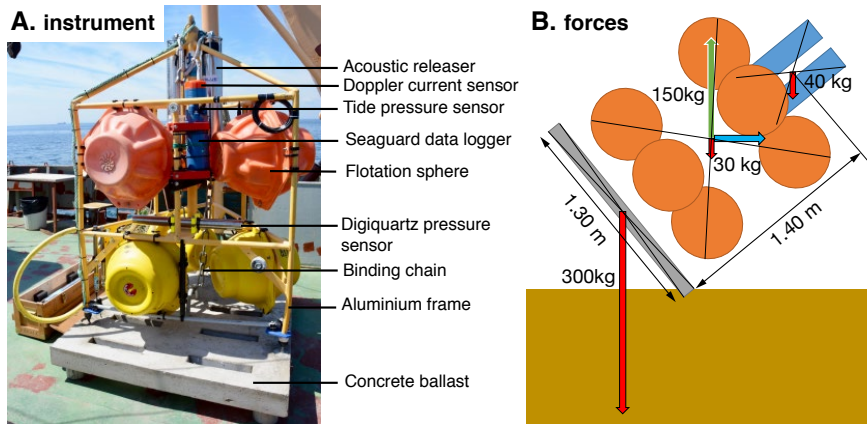


142 The instrumentation on the frame comprises (1) an RBR bottom pressure recorder
143 (BPR) with a Paroscientific 0-2000 m Digiquartz sensor, (2) a Seaguard recording
144 current meter (RCM) equipped with a Z-pulse 4520 Doppler current meter operating in
145 the 1.9-2 MHz frequency range and other sensors: temperature, pressure (tide sensor
146 Aanderaa 5217), conductivity (Aanderaa 4319), oxygen (Aanderaa optode 4330)
147 (Figure 2). The RBR pressure recording interval was set to 5s and that of the Seaguard
148 RCM to one hour for all sensors. The Doppler current meter worked in burst mode,
149 averaging 150 pings taken every second at the end of each one-hour recording interval.
150 The SeaGuard instrument was fixed on the upper part of the frame 1.5 m above the
151 seafloor and emit 4 narrow (2°) beams at orthogonal directions in a plane, parallel to
152 the seafloor if the frame is standing upright, and measures Doppler backscatter in cells
153 extending 0.5-to-2 meters from the instrument (Figure 3). The instrument was set in
154 forward ping mode, so that only data from sensors measuring a positive Doppler shift,
155 upstream currents moving toward the instrument, are used to calculate current speed.
156 The tide sensor is a piezoresistive sensor with a specified accuracy comparable to that
157 of the Digiquartz sensors (4kPa for a 0-2000 m sensor vs. 2kPa for a Digiquartz sensor
158 with the same range) and 0.2 hPa (2 mm) resolution and comprises a temperature
159 sensor of 0.2°C accuracy and 0.001°C resolution. The tide sensor averages pressure
160 measured at a 2 Hz sampling rate over 300 s at the end of each one-hour time interval.
161 the tide sensor was checked against an atmospheric reference between deployments
162 and found to have a minimal drift, less than 1 hPa.

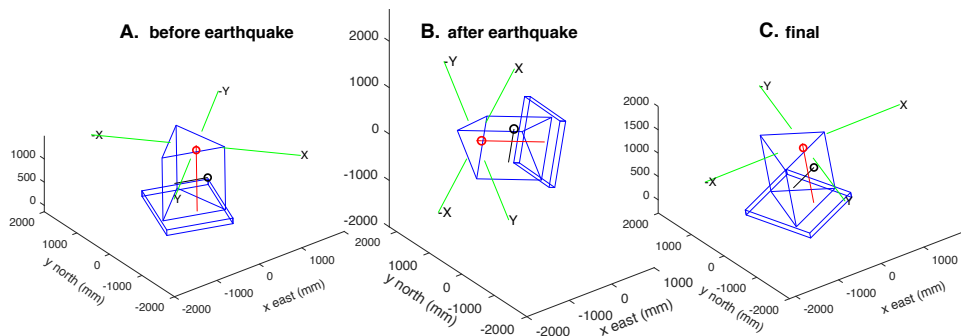
163 As we will show that the 09/24/2019 earthquake caused the instrumented device
164 to lay on its side for several hours and then straighten up, understanding the setup of
165 the seafloor device and its stability is important (Figure 2B). The frame is made of
166 aluminium and has 6 rigidly bound flotation spheres of 25 kg buoyancy each. The net
167 weight of the instrumented frame in water is -80 kg. The frame is rigidly attached to a
168 12-cm-thick 1.5x1.3 m concrete slab, weighting 300 kg in water. The assembly of the
169 heavy slab and buoyant frame is stable in upright position in the water and on the
170 seafloor. Moreover, it is estimated that a current of 1 m/s would cause a total horizontal
171 drag of 75 kg when the device is in upright position, which is insufficient to destabilize
172 it. If a stronger current, or other external forces, cause the assembly to tilt and lay on
173 one side, the moment of the gravity and buoyancy forces should straighten the device
174 back to upright position when these external forces are removed.



175 Measurement of current speed and direction by a tilted instrument is a related issue
176 that we here consider. The orientation and attitude of the Seaguard RCM is measured
177 with a 2-component accelerometer and a magnetic compass and the recorded data
178 include tilt in X and Y direction and the heading of the X axis. Tilt X and Y components
179 are factory calibrated from -35° to $+35^\circ$ with an accuracy of 1.5° . Tests performed in
180 the laboratory (see supplementary material, Figure S1) showed that tilt information
181 remains consistent outside this range, even when the instrument is upside down. Tilt
182 measurements are accurate within 3° up to 60° but saturate at about 80° (Figure S2).
183 Uncertainty on heading also increases with tilt, especially when the instrument is tilted
184 toward the X-direction. However, measured heading remains $\pm 20^\circ$ of true heading for
185 a tilting of up to 60° (Figure S3). The current measured in the instrument plane is
186 corrected for tilt assuming current is horizontal. As far as this approximation is valid,
187 the current record should in principle remain fairly accurate when the instrument is
188 tilted beyond the normal range of operation ($\pm 35^\circ$ degree) and at least to 60° . However,
189 the compass was not calibrated for an upside-down configuration. If the top of the
190 instrument would happen to be oriented downward, the measured current direction will
191 be unreliable, even though the absolute speed may still be correctly estimated. Another
192 problem may arise if one of the Doppler sensors is facing down into the sediment so
193 that its measurement cell is below the seafloor. If the sensor pointing upward in the
194 opposite direction is recording a negative Doppler shift, this value will be ignored in the
195 forward ping mode. In this case, the measurement retained to calculate current velocity
196 will correspond to noise from the sensor facing toward the seafloor. In all situations, it
197 remains possible to recalculate the sensor readings retained by the calculator from the
198 current velocity and orientation parameters recorded by the instrument, and thus
199 assess the reliability of data.
200



201
 202 **Figure 2.** Instrumented frame. (A) photo of the instrumented frame before
 203 deployment. (B) Sketch showing forces applied to the elements of the instrumented
 204 frame in water. The red arrows represent the weight in water of the cement ballast, of
 205 the instrumented frame and of the acoustic release system on top. The green arrow
 206 represents the buoyancy of the flotation spheres. The blue arrow represents the
 207 current drag, which depends on current speed and instrument tilt.
 208
 209



210
 211 **Figure 3.** Reconstruction of frame position based on instrument tilt-meter and
 212 compass data: (A) before the earthquake; (B) Tilted, between, 25 minutes and 10.5
 213 hours after earthquake; (C) back in nearly upright position 11 hours after earthquake.
 214 Position of Digiquartz pressure sensor (black circle), Aanderaa tide sensor (red
 215 circle) and Doppler current meter beam cells (green segments)
 216
 217



218 3. Results and interpretations

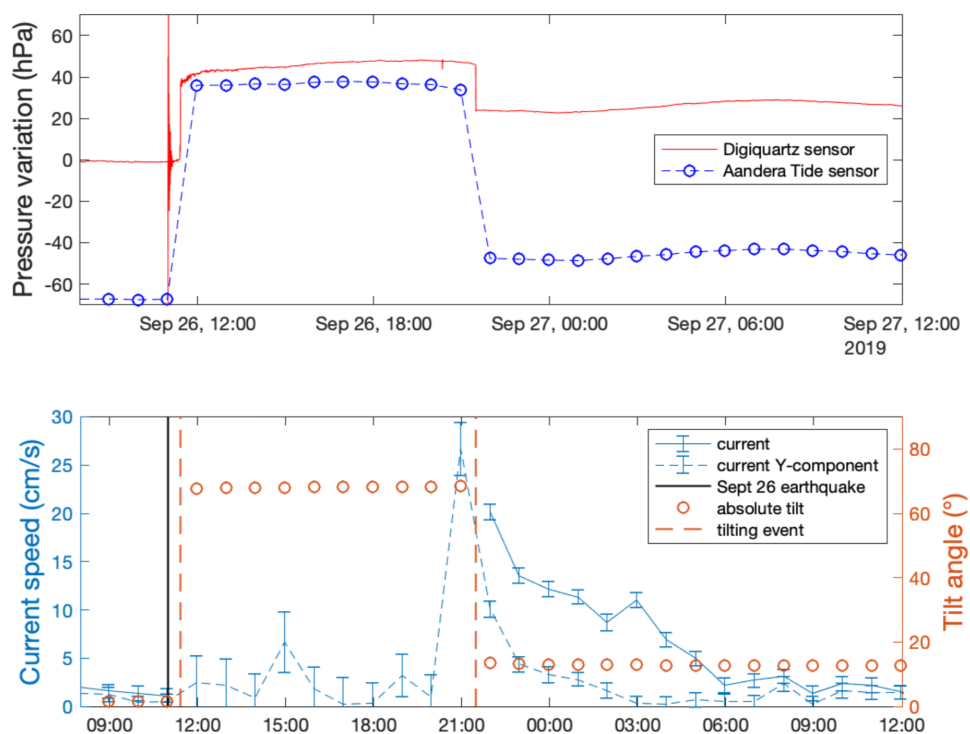
219 3.1. Pressure and tilt records

220 Pressure sensors are sensitive to pressure variations caused by P-waves and
221 Digiquartz sensors are also intrinsically sensitive to acceleration, but to a small extent,
222 160 hPa/g for an instrument with 20 MPa range according to the calibration report.
223 Small earthquakes are detected as pressure spikes, while oscillations are recorded
224 after large earthquakes. The M_w 4.7 09/24/2019 caused a short pressure transient of
225 25 hPa at 08:00:26 followed by small pressure oscillations of less than 3 hPa amplitude
226 decaying over a few minutes. The seismic wave train from the M_w 5.8, 09/26/1919
227 earthquake is recorded by the Digiquartz pressure sensor as oscillations, initiated by
228 a pressure drop of 65 hPa between 10:59:22 and 10:59:26 (Figure 4). For the sampling
229 interval of 5s used in this setup, the recorded signal is aliased, which precludes
230 quantitative interpretation in term of velocity or acceleration. However, the initial
231 pressure drop after the 09/26/1919 earthquake may indicate a negative polarity of the
232 first P arrival at the instrument site, located on an ascending ray-path.

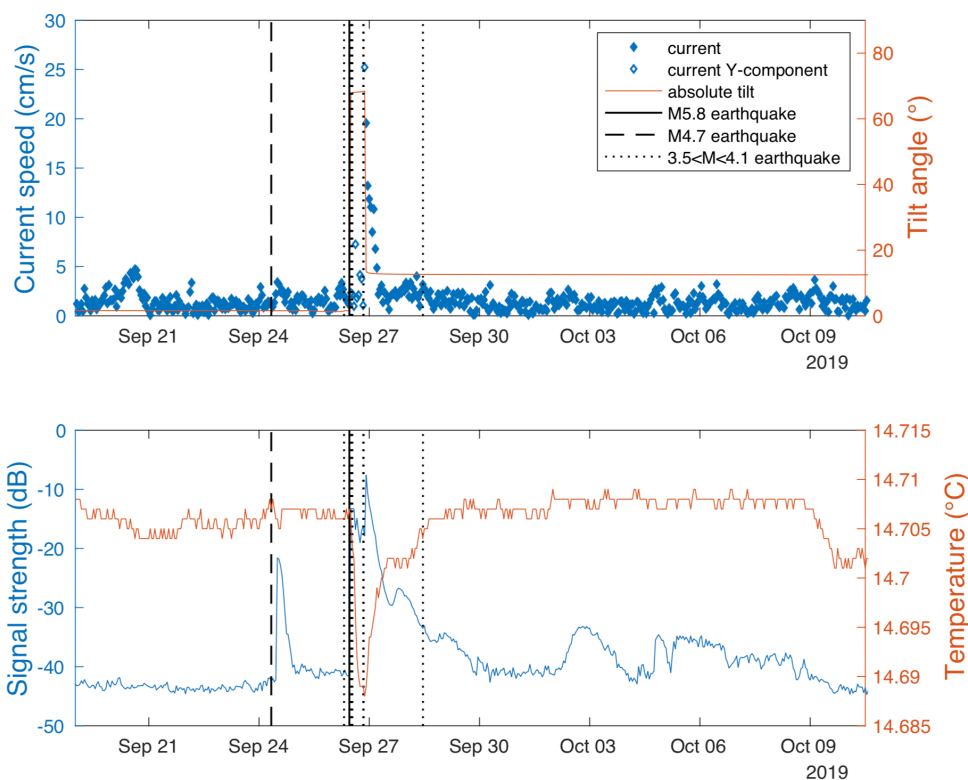
233 Twenty-five minutes after the M_w 5.8, earthquake, a new disturbance of the
234 pressure sensor is observed at 11:23:41. The pressure then progressively increases
235 by 30.9 hPa in 15 seconds between 11:24:46 and 11:25:01 before stabilizing. Over the
236 corresponding one-hour-time-interval between successive records, the Seaguard
237 RCM, initially subvertical (tilt less than 2°), acquires a strong tilt (Figure 3). At 11:57:48,
238 measured tilt is -65° along the X-axis and $+19^\circ$ along the Y-axis, with X-axis in a $N161^\circ$
239 azimuth and these values remain constant $\pm 2^\circ$ over the next 10 hours, corresponding
240 to an absolute tilt of 68° (Figure 4). The tilting of the instrument causes the Digiquartz
241 and Tide sensors to record different pressure variations because they are located at
242 different positions on the frame (Figure 2). Moreover, the pressure readings by the
243 Digiquartz sensor also depend on its orientation relative to Earth gravity. Pressure at
244 the Tide sensor location increases about 100 kPa, corresponding to a 1 m drop and
245 indicating that the frame was then practically laying on its side. Ten hours later, the
246 device apparently straightens itself in about 5 seconds, between 21:28:29 and
247 21:28:34 as indicated by a rapid pressure variation. After that, the recorded tilt
248 parameters are moderate and stabilize at -11.5° for the X-axis and 5.3° for the Y-axis,
249 with X-axis in a $N105.3^\circ$ azimuth.



250 The M_w 4.7 earthquake caused minor disturbances of the attitude of the
251 instrument, with variations of tilt and heading of less than 0.5° . A M_w 3.6 foreshock of
252 the M_w 5.8 occurring 26/09/2019 at 7:32 also caused minor disturbances. These
253 indicate that the seafloor was sensitive to ground shaking caused by these small
254 earthquakes, however, this did not cause the device to sink into the sediment. Changes
255 of pressure baseline of the digiquartz sensor between before and after these
256 earthquake are difficult to resolve, and correspond to less than 5 mm vertical
257 displacement for the first event and less than 2 mm for the second one.
258



259
260 **Figure 4.** Time series around the time of occurrence of a M_w 5.8 earthquake; (top)
261 pressure variations recorded by two instruments on the instrumented frame; (bottom)
262 current and tilt data recorded by Seaguard RCM. Between the tilting events only one
263 component of the doppler current meter functioned reliably (Y-component oriented
264 N200) and is here reported.



265
266 **Figure 5.** Time series acquired with Seaguard RCM during the September 2019
267 seismicity cluster; (top) current speed and tilt; (bottom) backscatter signal strength
268 and temperature.

269

270 3.2. Current records and possible causes of tilting

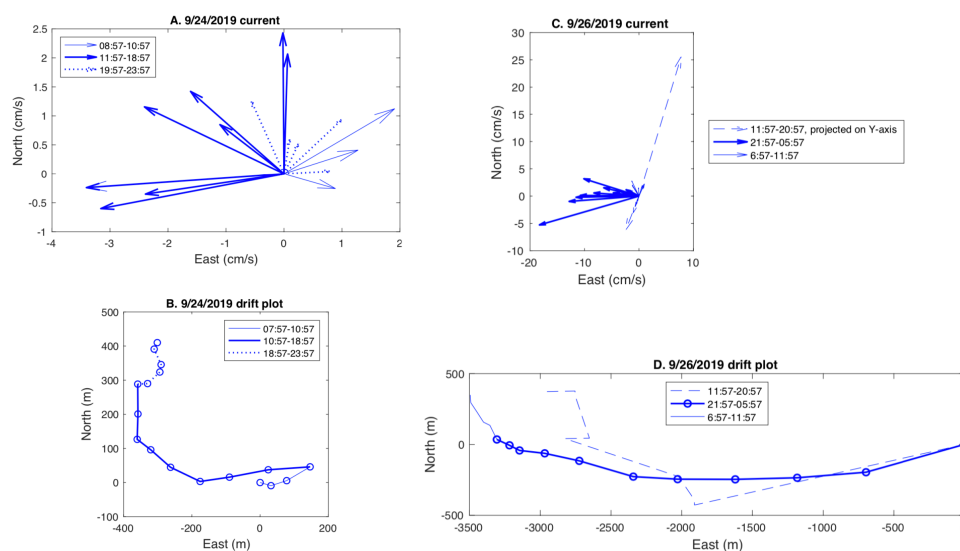
271 The M_w 4.7 09/24/2019 earthquake was followed by a small increase of current
272 strength peaking at 3.4 cm/s at noon, 4 hours after the earthquake (Figure 5).
273 Comparable events in term of duration and strength occurred spontaneously
274 09/20/2019 (with currents up to 4.7 cm/s) and 09/26/2019 just before the main
275 earthquake. During all three events the dominant current was from the east, thus
276 coming from the direction of the canyon, but there is an important difference between
277 the event that occurred after the earthquake and the two others. During that event a
278 change in current direction occurred from eastward to westward between 10:57 and
279 11:57 while the current strength increased from 2.2 cm/s to its peak value (Figure 6).
280 During the other events, build-up was more progressive and did not involve a change
281 in direction. A drift plot, calculated by summing velocity vectors over time, reproduces



282 the motion of a particle assuming a uniform velocity field (Figure 6). The total drift is
283 about 500 m and occurs in the 8 hours following the current inversion. Current direction
284 varies from Westward to Northward during this time interval.

285

286



287

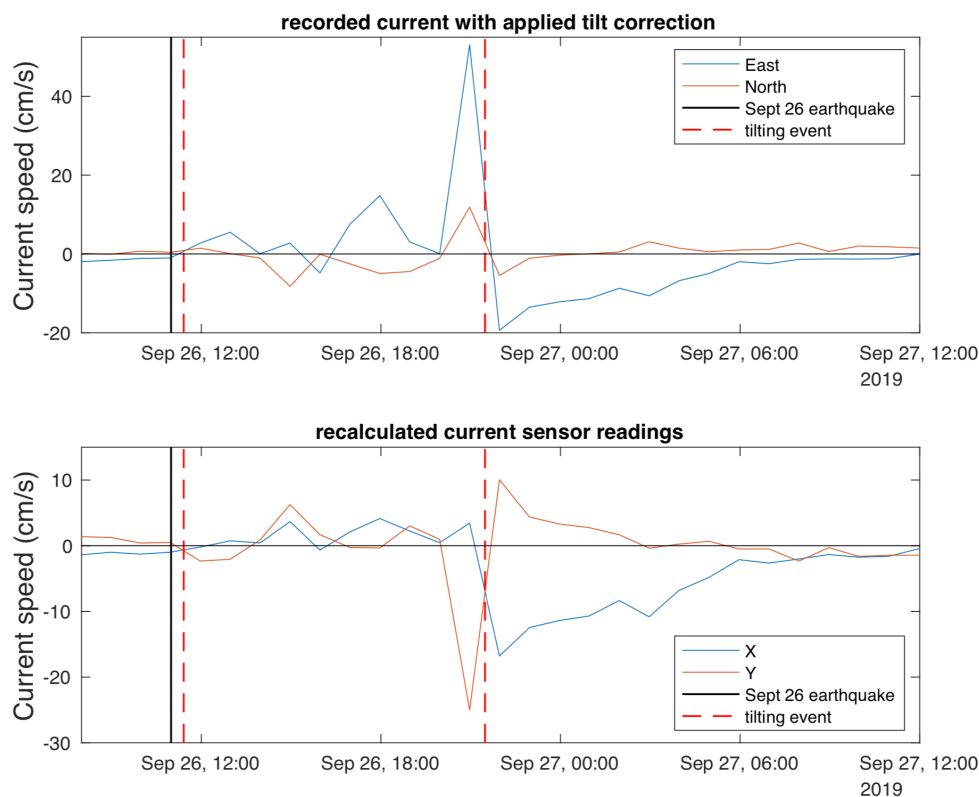
288 **Figure 6.** Current recorded after M_w 4.7 and M_w 5.8 earthquakes: (A) Current velocity
289 arrows recorded every hour between 08:57 and 23:57 on 09/24/2019; (B) drift plot
290 over the same time interval, the change of current direction and strength between
291 10:57 and 11:57 coincides with increasing backscatter strength (see figure 4),
292 indicative of increased turbidity; (C) Current velocity arrows recorded every hour
293 between 12:00 09/26/2019 and 06:00 09/27/2019. Dashed arrows show
294 measurements acquired in the Y direction when the instrument was strongly tilted
295 (position B in Figure 3), plain arrows when it was back in upright position (C in Figure
296 3); (D) drift plot over the same time interval, the dashed part corresponds to the
297 strongly tilted position.

298

299 After the M_w 5.8 09/26/1919 earthquake, during the 10 hours period when the
300 instrument remained strongly tilted, the instrument recorded currents varying both in
301 speed and orientation, but some precautions are needed when interpreting these data.
302 The current component measured by transducers along the Y-axis of the instrument,
303 oriented $N200^\circ$, probably remained accurate as the tilt along this axis is less than 20°



304 and the measurement cell remained above the bottom (Figure 2B). On the other hand,
305 the X-component may not be reliable as one of the sensors ($n^{\circ}1$) is oriented 65°
306 upward in the $N160^{\circ}$ direction, and the opposite sensor ($n^{\circ}3$) is dipping 65° downward
307 in the opposite ($N340^{\circ}$) direction. Consequently, measurement cell $n^{\circ}3$ lies within the
308 sediment and thus may only record noise. Moreover, because the Doppler current
309 sensor (DCS) is set in forward pinging mode, current speed is calculated with data
310 from sensors measuring positive doppler shifts only. This implies that if the current
311 component toward $N160^{\circ}$ is positive, sensor $n^{\circ}1$ will measure a negative shift and will
312 not be recorded. During the time interval here considered, the measured current
313 component in the X-direction (toward $N160$) is positive, which indicates that data from
314 sensor $n^{\circ}4$ was used (Figure 7), and that is probably noise. It follows that the current
315 component along the Y-direction is the only one reliable. The horizontal current
316 measured along the Y-axis changed sign several times during this time interval, and
317 reached peak values of 6.3 cm/s toward $N200$ at $14:57:46$, about four hours after the
318 earthquake, and of 25 cm/s in the opposite direction at $20:57:46$, the last measurement
319 before the instrument straightened up. Other measurements on both axes remain
320 below 5 cm/s , but the absolute velocity may have been higher because this
321 measurement was only performed in one direction. Yet, these observations suggest
322 that the strong current recorded before the instrument straightened up played a role
323 in this event. Once the device got back in an upright position, it recorded a current
324 consistently flowing westward and progressively decreasing from 20 cm/s to
325 background level (2 cm/s) in 9 hours (Figure 4). During this waning phase, the current
326 drift is about 3.5 km in a westward direction (Figure 6). The drift estimated during the
327 first 10 hours after the earthquake, while the instrument was strongly tilted, is in the
328 opposite direction but may not be reliable.
329



330

331 **Figure 7.** Current record acquired around the time of occurrence of a M_w 5.8
332 earthquake. A. Instrumental record, automatically corrected for tilt and heading. B.
333 recalculated readings in the X and Y axis of the Doppler sensor (see text for
334 interpretation).

335

336 The current speed in the first 2 hours after the main earthquake apparently
337 remained low, at most 5-6 cm/s. It is thus unlikely that the tilt of the device was caused
338 by strong currents. Some short burst of current may have been missed because of the
339 1 hour sampling interval, but this would not explain why the frame then remained stable
340 in a tilted position for several hours. Local liquefaction of the sediment beneath the
341 device is also an unlikely cause because the tilting of the instrument occurred 25
342 minutes after the earthquake. A mud flow originating from the basin slopes thus
343 appears as a more likely cause. This hypothesis would also account for the presence
344 of sandy mud caked on the device in various places: on the frame feet, on the acoustic
345 releasers, on the optode connector and also inside the plastic protection of a flotation



346 sphere, from which bindings were broken and had to be repaired. On the other hand,
347 the current speed in the 20-50 cm/s range recorded before, as well as after, the time
348 when the device straightened up is strong enough to cause erosion of mud or sand
349 deposits. It may thus be hypothesized that erosion freed the device from the mud cover.
350 The flotation spheres on the frame and the concrete ballast at its base exert a moment
351 that should keep the assembly stable in an upright position unless the frame is loaded
352 with sediment.

353

354 3.3. Acoustic backscatter record

355 The strength of the backscattered signal can be used as a proxy for turbidity.
356 The Seaguard RCM emits in the 1.9-2 MHz band corresponding to a wavelength (λ) of
357 750 μm . Doppler backscatter current meters have maximum sensitivity for particles of
358 diameter $D = \lambda/\pi$ and can detect particles down to diameter $D = 0.08 \lambda$, for which
359 backscatter power is less than 1/10 of peak backscatter power (Guerrero et al., 2011,
360 2012). The seaguard RCM should thus be mostly sensitive to the presence in
361 suspension of sand size particles (larger than 63 μm). The background backscatter
362 amplitude level is $-43 \pm 1 \text{ dB}$ before the earthquakes. Three to four hours after the M_w
363 4.7 09/24/2019 earthquake, backscatter increases sharply to -22 dB between 11:00
364 and 12:00, and then decays to -41 dB in 12 hours. The increase of backscatter
365 coincides with a change of current direction and speed, indicating that the turbid cloud
366 was brought to the instrument site by the current. However, the current speed of less
367 than 4 cm/s may have been insufficient to put the particles in suspension. There is no
368 increase of backscatter on Sept 20 when stronger currents coming from the same
369 direction, but not related with an earthquake, were recorded.

370 Backscatter strength remain $41 \pm 1 \text{ dB}$ the 1.5 days interval before the M_w 5.8
371 09/26/1919 and increases to the -20 dB to -13 dB range after the earthquake (Figure
372 5), which implies sand sized sediment was put in suspension soon after the earthquake
373 although the local current speed remained relatively low (about 5 cm/s at most). After
374 the device went back to near vertical position, signal strength reaches a maximum of -
375 7.6 dB, which correspond to an amplitude ratio of 42 and an intensity ratio of 1800
376 compared to base level. Similar signal strength levels are typically reached with the Z-
377 Pulse sensor in highly turbid water such as in estuaries. During deep sea deployments
378 signal strength range more typically between -60 and -40 dB . After reaching peak value,



379 backscattered signal strength progressively decays to stabilise at about -40 dB 3 days
380 (Figure 5). Several turbid events, with signal strength about -35 dB are observed in
381 October and associated with small increases in current velocity (up to 3-4 cm/s). It is
382 unclear whether these passing clouds are residual turbidity from the earthquake. After
383 October 9, backscatter eventually returns to background level while temperature
384 decreases by 0.007 °C over a few hours, indicating replacement of the water mass
385 around the instrument.

386

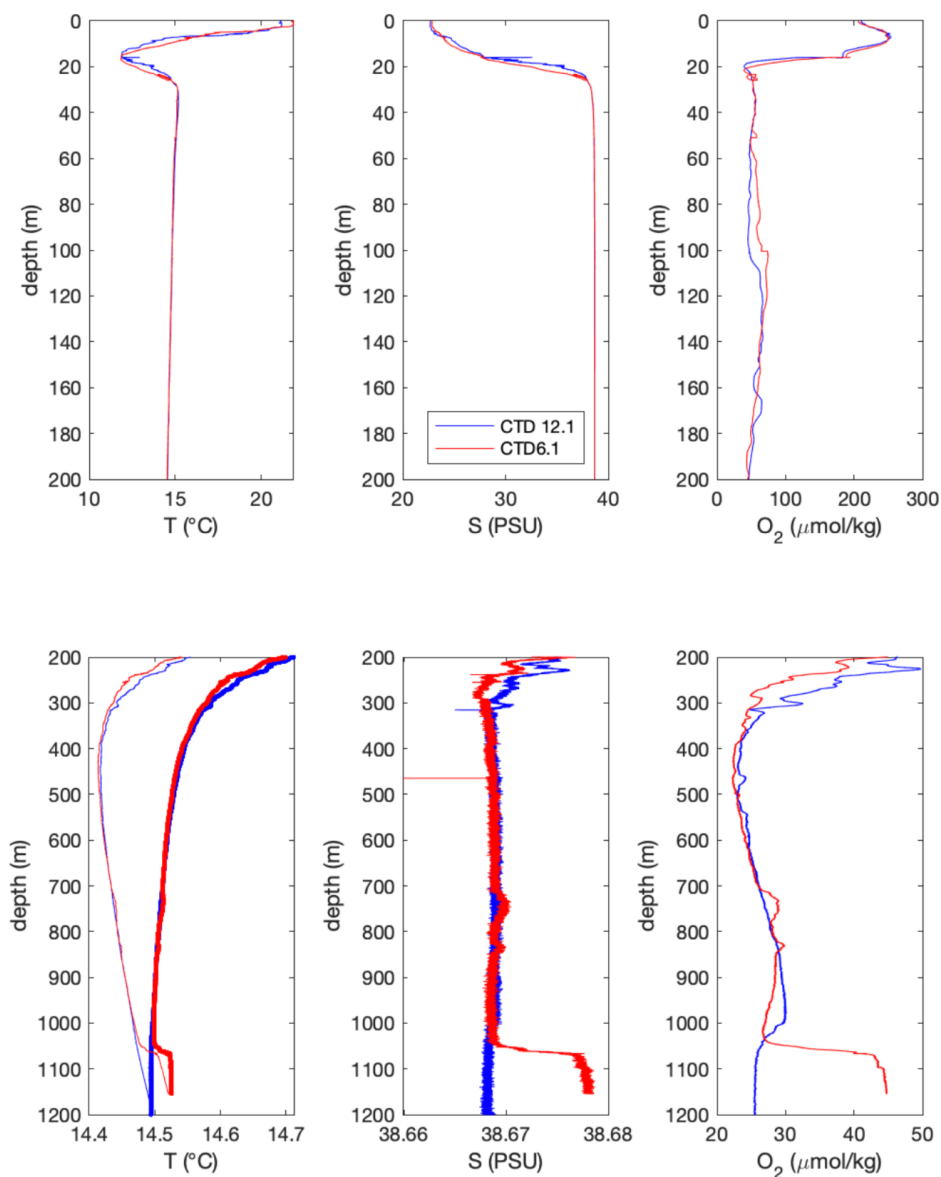
387 3.4. Temperature record

388 The Sea of Marmara is stratified, with a low salinity (20-22‰) 20-30 m surface
389 layer that displays strong seasonal temperature variability overlaying a high salinity
390 (about 38‰) body of seawater at 14-15°C derived from the Aegean Sea (Beşiktepe et
391 al., 1994). Within this body, the potential temperature generally decreases with depth,
392 which would in principle imply that a turbidity current, flowing downward, should cause
393 a small temperature increase. However, the deployment site is prone to seasonal
394 cascading, so that the initial temperature structure may have been disturbed. Example
395 of CTD profiles recorded in June 2007 (Henry et al., 2007) are shown in Figure 8. No
396 CTD profile is available in Sept 2019, but variations in temperature and oxygen
397 concentration associated with mild currents (<5 cm/s) were recorded by the instrument
398 in May-July 2019, and again on Sept 20.

399 Temperature variations associated with the M_w 4.7 09/24/2019 earthquakes are
400 very small, less than $\pm 0.002^\circ\text{C}$, which confirms that water did not travel far during this
401 event. After the M_w 5.8 09/26/1919 earthquake, the recorded temperature decreases
402 progressively by about 0.015°C , after the first hydrologic disturbance and tilting of the
403 instrument, until the recorded current reaches its maximum value (Figure 5).
404 Temperature then progressively increases to reach nearly the same value as before
405 the event. The small variation in temperature recorded indicates that the turbid water
406 originates from the deep-water body. The slight temperature decrease observed after
407 the earthquake can result from the mixing of a warmer bottom water layer with the bulk
408 of the deep-water layer. However, the observation of a temperature drop precludes
409 that the turbid water originates from depths less than 400 m, as water present between
410 400 m and the halocline is at a higher potential temperature than the deeper water
411 throughout the year (see Beşiktepe et al., 1994, and figure 8). Moreover, an inflow of



412 water from closer to the surface should result in an increase in the O₂ concentration in
413 the bottom water, but none is observed in the data.
414



415
416 **Figure 8.** Depth plots of Temperature (°C), Salinity (PSU) and oxygen concentration
417 (μmol/kg) from CTD profiles acquired in the Sea of Marmara during Marnaut cruise of
418 Ifremer RV L'Atalante (Henry et al., 2007). On the lower temperature plot, thin lines



419 are measured values and thick lines are potential temperatures calculated at 1180 m.
420 Locations are shown on Figure 1

421

422 3.5. Inferred sequence of events

423 These observations provide some insight on the complex sequence of events
424 that followed the earthquake and suggest the following scenario. After the M_w 4.7
425 09/24/2019 a turbid cloud formed east of the instrument and drifted slowly. Considering
426 the maximum velocity of the current (less than 4 cm/s) and the 4-hours interval
427 between the earthquake and the passing of the turbid cloud over the instrument, the
428 front of turbid water should have formed ENE of the instrument at a maximum distance
429 of about 500 m, and this coincides with the base of the northern slope near the outlet
430 of the canyon. It is suspected that instability on the steeper slopes on the sides of the
431 canyon is the primary cause of sediment suspension. The clouds subsequently drifted
432 downslope over a total horizontal distance of at most 1 kilometers before dissipating,
433 adding the 500 m estimate above to the drift calculated after the passing of the front
434 over the instrument (Figure 6).

435 The M_w 5.8 09/26/1919 caused much stronger currents. After the passing of
436 the seismic wave, triggering of instability on slopes adjacent to the deployment site
437 caused mud flows that spread on the basin floor causing the tilting of the instrument
438 25 minutes after the earthquake, and bottom water turbidity. As the base of the nearest
439 slope is about 400 m north of the instrument, this would imply a minimum velocity of
440 20 cm/s for the mudflow to reach the device location in 25 minutes. During the following
441 10 hours, the current record is incomplete but indicates variations in strength and
442 direction. Widespread slope instabilities triggered by the earthquake may have resulted
443 in several turbidity currents recorded as successive pulses. The role of seiches and
444 surface gravity waves in sediment resuspension can be ruled out as no tsunami was
445 recorded by near shore tidal gauges around the Sea of Marmara. The relationship
446 between gravity wave amplitude A and bottom current amplitude U in the shallow water
447 linear approximation is given by $U=(g/H)^{1/2}A$, where H is water column height. An
448 oscillatory current of 10 cm/s at 1200 m depth would thus correspond to a free surface
449 oscillation of 1 m (or 100 hPa) for a standing wave (seiche) as well as a progressive
450 wave (tsunami). This should have been easily detected in a sea where tidal amplitude
451 is about 10 cm (Alpar and Yüce, 1998). The influence of baroclinic internal waves on



452 the halocline at 20-30 m depth must also be ruled out as they cannot physically
453 produce currents of more than a few cm/s at 1200 m. However, It remains possible
454 that the interface at the top of the turbid cloud is affected by baroclinic waves. The
455 strongest current is recorded after 10 hours, which suggests that a turbidity current
456 initiated further upslope may have reached the site after a longer delay but may also
457 have gained more kinetic energy on its downhill path. This event, reaching a speed
458 exceeding 25 cm/s apparently caused enough erosion to free the device from the mud
459 accumulation. The current then stabilizes in a westward direction and decays
460 progressively over the next 9 hours, which suggests the tail of a turbidity current flowing
461 in the canyon E of the deployment site has been recorded. The hours-long delay
462 between the earthquake and the passing of the fastest current over the instrument may
463 hypothetically correspond to the time for the head of the turbidity current to travel from
464 its source to the location of the instrument. The length of the canyon valley between
465 the device location and the 400 m isobath, inferred to be the minimum depth of the
466 turbid water source, is about 13 km. In this scenario, the average velocity of the head
467 of the turbidity current would be 30-40 cm/s. Alternatively, a sequence of slope failures
468 may have lasted up to several hours after the earthquake. The distance travelled by
469 the turbidity current on the basin floor beyond the instrument may be estimated from
470 the calculated drift during the waing phase, and is found to be about 3.5 km (Figure 6).
471 When plotted over the bathymetric map the drift appears to stay within the depositional
472 fan at the outlet of the cayon, the extension of which is known from sediment sounder
473 profiles (Figure 1). These calculations are only a rough estimate of the distance
474 travelled by suspended particles as only the velocity at 1.5 m above the seafloor is
475 known. However, it appears unlikely that sediments spread all over the 15x20 km basin
476 floor as this would require velocities of the order of 1m/s, sustained over a wide area
477 for several hours.

478 The decay of the backscatter signal strength over the next 3 days may reflect
479 the settling of sand size particles put in suspension in the water column after this
480 sequence of events. For a first order assessment, Stokes settling velocity, an upper
481 bound valid in dilute suspensions (e.g. Guazelli and Morris, 2012) may be used. The
482 Stokes settling velocity of 63 μm quartz grains (density 2650 kg/m^3) in 13°C seawater
483 is 2.7 mm/s, allowing such grains to drop by 700 m in 3 days. However, if the particles
484 forming the cloud are mostly composed of clay agregates, which density may be
485 comprised between 1200 and 1700 kg/m^3 , the settling velocity would be comprised



486 between 0.3 mm and 1 mm/s. In this case the height of the suspended particle cloud
487 could range between 70 and 250 m.

488 4. Discussion and conclusion

489 Data obtained with a seafloor device located at the outlet of a canyon in the
490 Central Basin in the Sea of Marmara bring some insight on how earthquakes scale
491 with their hydrodynamic consequences. In September 2019, M_w 4.7 and 5.8
492 earthquakes occurred at a 5 km distance from the device as well as a series of smaller
493 foreshocks and aftershocks. In this setting, earthquakes of magnitude less than 4 did
494 not cause noticeable water column turbidity nor currents. The M_w 4.7 earthquake
495 generated a turbid cloud on slopes a few hundred meters from the instrument and the
496 cloud took 3-4 hours to drift down to the instrument location and 10 more hours to
497 dissipate. As the current velocity remained small (less than 4 cm/s), it can be concluded
498 that this cloud did not evolve into a self-sustained turbidity current (Parker, 1982). The
499 M_w 5.8 earthquake initiated a turbidity current and the data obtained may be compared
500 with more complete records of turbidity currents obtained elsewhere with ADCP
501 deployments and/or water column mooring lines. The duration of the event in the Sea
502 of Marmara (about 10 hours) appear fairly typical and comparable with events recorded
503 in other locations regardless of the initiation mechanism, which comprise hyperpycnal
504 flows from river floods (Var and Gaoping canyons), storm waves and dredging (Gulf of
505 St Laurence and Monterey canyon), and slope instabilities triggered by an earthquake
506 (Tokachi-oki) or by other processes (Var canyon) (Normandeau et al., 2019;
507 Khripounoff et al., 2012; Xu et al., 2004; Liu et al., 2012; Mikada et al., 2006). Longer
508 duration events with very different hydrodynamic characteristics have been observed
509 in larger scale systems (e.g. Congo deep sea canyon, Azpiroz-Zabala et al., 2017). On
510 the other hand, events recorded closer to shore on the edge of the continental shelf or
511 on a delta front have much shorter durations (Xu et al., 2010; Hughes Clarke, 2016).
512 In events of comparable scale to the Sea of Marmara one, the velocity of the current
513 generally reaches its maximum several meters above the seafloor, so that the velocity
514 recorded by our instrument at 1.5 m from the seafloor is within the boundary layer, and
515 lower than either the maximum current velocity or the velocity of the head of the
516 turbidity current. A velocity of several tens of centimeter per second is representative
517 of the slower recorded examples, corresponding to mud rich flows associated with
518 hyperpycnal flows, to the smaller landslides (Khripounoff et al. 2012) or to the smaller



519 storm-related events (Normandeau et al., 2019). Turbidites following large
520 earthquakes or large slope instabilities have reached maximum velocities of 20 m/s
521 (Piper et al., 1999). Velocities of 2-7 m/s were reported for the turbidity current following
522 Tohoku earthquake (Arai et al., 2013) and 1.4 m/s in the Tokachi-Oki case (Mikada et
523 al., 2006). The downward current after the off-Izu Peninsula earthquake may be
524 constrained with a noisy ADCP record to a maximum of 10-15 cm/s in a 20-30 m layer
525 above the seafloor and lasted about one hour, peaking about 30 minutes after the
526 earthquake (Kasaya et al., 2009). This turbidity current thus appears less intense and
527 shorter in duration than the one recorded in the Sea of Marmara, but the triggering
528 earthquake was also smaller (M5.4 compared to M5.8) and more distant (10 km).
529 These observations suggest that a general scaling relationship could exist between
530 earthquake magnitudes and the strength and extent of the turbidity currents they
531 induce. Moreover, although the off-Izu event is shorter than the Sea of Marmara one,
532 they share an important characteristic in that the turbid cloud is observed to form when
533 a mud flow hits the observatory site and some time before current builds up in the
534 water column.

535 The 10 hours delay observed in the Sea of Marmara between the triggering
536 event and the peak of the turbidity current is long compared to the 2 hours delay
537 observed after Tohoku and Tokachi-oki earthquakes. We suggested earlier that the
538 long delay may simply result from a slower velocity of the turbidity current or from
539 delayed slope failure. Another possibility is delayed ignition, which may occur if the
540 turbidity current develops indirectly from the hydrodynamic instability of a turbid cloud
541 resulting from slope failures and/or ground shaking rather than by acceleration of a
542 dense mud flow (Parker, 1982; Mulder and Cochonnat, 1996; Piper and Normark,
543 2009).

544 The scenario we propose for the Sept 26, 2019 earthquake involving mud flows
545 from proximal sources, followed by turbidity currents originating at larger distances,
546 and the subsequent settling of sediment in suspension, could relate with the structure
547 of turbidite-homogenites. Progressive or pulsed build-up of turbidity current energy is
548 considered typical of hyperpycnal flows initiated by river floods (Mulder et al., 2003)
549 but reverse grading and pulsing is also observed in seismoturbidites (Gutierrez-Pastor
550 et al., 2013). In the Sea of Marmara, many of the laminated turbidites sampled in
551 Kumburgaz Basin formed from the amalgamation (below the homogenite layer) of at
552 least two flows, the first one being finer and less sorted (Yakupoglu et al., 2019). The



553 coarsening observed in this context is often associated with an increase of the calcium
554 content indicative of a shallower source, rich in biogenic carbonate material. However,
555 in the case observed in the present study, remobilization of sediment should be limited
556 to the lower slope as the temperature of the displaced water precludes a source
557 shallower than 400 m water depth.

558 The geomorphological context of the deployment site south of a slope identified
559 as unstable from geomorphological criteria (Zitter et al., 2012), and on a depositional
560 fan at the outlet of a canyon is also consistent with the proposed scenario. We
561 estimated by integrating recorded current velocity that the current during this event
562 was not strong enough to spread the sediment over the entire Central Basin floor but
563 that the zone of deposition was probably comparable in size to the fan. It can be
564 inferred that the paleoseismological record from a core taken in the fan should contain
565 more events than one taken at the basin depocenter. A sediment sounder profile
566 (Figure 1) also shows that the character of the seismic reflectors differs in the basin
567 and in the fan and that establishing reliable correlations between them is not simple.
568 However, as hypothesized by previous studies (McHugh et al., 2014), turbidite-
569 homogenite deposits that can be correlated between cores taken at various locations
570 in the basin probably correspond to the larger events, which may be correlated with
571 historical earthquakes. Moreover, it is still unknown whether the Sept 26 event left a
572 trace on the seafloor morphology and in the sediment record. Performing new core
573 sampling and very high-resolution geophysical surveys in this area would thus have
574 important implications for the understanding of seismoturbidite records and for the
575 assessment of geohazards.

576

577 Acknowledgements

578 Financial support was provided by the bilateral ANR/TÜBITAK collaborative research
579 project MAREGAMI (ANR-16-CE03-0010-02 and Tübitak Project 116Y371) and by
580 CNRS-INSU through the European Multidisciplinary Sea Observatory (EMSO)
581 Research Infrastructure program. DT-INSU and Istanbul Technical University
582 hydrodynamic engineering department provided technical support for device design,
583 construction, and deployment. Bernard Mercier de Lépinay provided processed
584 sediment sounder profiles. We thank the crew and Captain of R/V Yunus (Istanbul
585 University) for their support during installation and recovery of the instruments.



586 Seafloor monitoring data are available through SEANOE (Henry et al., 2021) and
587 CTD profile data through SISMER Oceanographic Data portal (Henry et al., 2007).
588

589 References

- 590 Alpar, B., & Yüce, H. (1998). Sea-level variations and their interactions between the Black
591 Sea and the Aegean Sea. *Estuarine, Coastal and Shelf Science*, 46, 609–619.
- 592 Arai, K., Naruse, H., Miura, R., Kawamura, K., Hino, R., Ito, Y., Inazu, D., Yokokawa, M.,
593 Izumi, N., Murayama, M., & Kasaya, T. (2013). Tsunami-generated turbidity current of
594 the 2011 Tohoku-Oki earthquake. *Geology*, 41(11), 1195–1198.
595 <https://doi.org/10.1130/G34777.1>
- 596 Armijo, R., Meyer, B., Navarro, S., King, G., & Barka, A. (2002). Asymmetric slip partitioning
597 in the Sea of Marmara pull-apart: a clue to propagation processes of the North Anatolian
598 Fault? *Terra Nova*, 14(2), 80–86. <https://doi.org/10.1046/j.1365-3121.2002.00397.x>
- 599 Armijo, R. and J. Malavieille (2002) MARMARASCARPS cruise, RV L'Atalante,
600 <https://doi.org/10.17600/2010140>
- 601 Azpiroz-Zabala, M., Cartigny, M. J. B., Talling, P. J., Parsons, D. R., Sumner, E. J., Clare, M.
602 A., Simmons, S. M., Cooper, C., & Pope, E. L. (2017). Newly recognized turbidity current
603 structure can explain prolonged flushing of submarine canyons. *Science Advances*,
604 3(10). <https://doi.org/10.1126/sciadv.1700200>
- 605 Beck, C., Mercier de Lépinay, B., Schneider, J. L., Cremer, M., Çağatay, N., Wendenbaum,
606 E., et al. (2007). Late Quaternary co-seismic sedimentation in the Sea of Marmara's
607 deep basins. *Sedimentary Geology*, 199, 65–89.
608 <https://doi.org/10.1016/j.sedgeo.2005.12.031>
- 609 Beşiktepe, Ş. T., Sur, H. İ., Özsoy, E., Latif, M. A., Oğuz, T., & Ünlüata, Ü. (1994). The
610 circulation and hydrography of the Marmara Sea. *Progress in Oceanography*, 34(4),
611 285–334. [https://doi.org/10.1016/0079-6611\(94\)90018-3](https://doi.org/10.1016/0079-6611(94)90018-3)
- 612 Brizuela, N., Filonov, A., & Alford, M. H. (2019). Internal tsunami waves transport sediment
613 released by underwater landslides. *Scientific Reports*, 9(1), 10775.
614 <https://doi.org/10.1038/s41598-019-47080-0>
- 615 Bulut, F., Aktuğ, B., Yalıtırak, C., Doğru, A., & Özener, H. (2019). Magnitudes of future large
616 earthquakes near Istanbul quantified from 1500 years of historical earthquakes, present-
617 day microseismicity and GPS slip rates. *Tectonophysics*, 764(July 2018), 77–87.
618 <https://doi.org/10.1016/j.tecto.2019.05.005>
- 619 Çağatay, M. N., Erel, L., Bellucci, L. G., Polonia, a., Gasperini, L., Eriş, K. K., Sancar, Ü.,
620 Biltekin, D., Uçarkuş, G., Ülgen, U. B., & Damci, E. (2012). Sedimentary earthquake



- 621 records in the İzmit Gulf, Sea of Marmara, Turkey. *Sedimentary Geology*, 282, 347–359.
622 <https://doi.org/10.1016/j.sedgeo.2012.10.001>
- 623 Çaçatay, N. M., Uçarkus, G., Eris, K. K., Henry, P., Gasperini, L., & Polonia, A. (2015).
624 Submarine canyons of the Sea of Marmara. In F. Briand (Ed.), *Submarine Canyon*
625 *Dynamics in the Mediterranean and Tributary Seas*, CIESM Workshop Monograph n° 47
626 (pp. 123–135). CIESM Publisher, Monaco. <https://doi.org/10.13140/RG.2.1.1692.8402>
- 627 Cattaneo, A., Babonneau, N., Ratzov, G., Dan-Unterseh, G., Yelles, K., Bracane, R., Mercier
628 De Lapinay, B., Boudiaf, A., & Deverchere, J. (2012). Searching for the seafloor
629 signature of the 21 May 2003 Boumerdas earthquake offshore central Algeria. *Natural*
630 *Hazards and Earth System Science*, 12(7), 2159–2172. <https://doi.org/10.5194/nhess->
631 [12-2159-2012](https://doi.org/10.5194/nhess-12-2159-2012)
- 632 Dan, G., Sultan, N., Savoye, B., Deverchere, J., & Yelles, K. (2009). Quantifying the role of
633 sandy-silty sediments in generating slope failures during earthquakes: Example from the
634 Algerian margin. *International Journal of Earth Sciences*, 98(4), 769–789.
635 <https://doi.org/10.1007/s00531-008-0373-5>
- 636 Drab, L., Hubert Ferrari, A., Schmidt, S., & Martinez, P. (2012). The earthquake sedimentary
637 record in the western part of the Sea of Marmara, Turkey. *Natural Hazards and Earth*
638 *System Science*, 12(4), 1235–1254. <https://doi.org/10.5194/nhess-12-1235-2012>
- 639 Drab, L., Hubert-Ferrari, A., Schmidt, S., Martinez, P., Carlut, J., & El Ouahabi, M. (2015).
640 Submarine Earthquake History of the Çınarcık Segment of the North Anatolian Fault in
641 the Marmara Sea, Turkey. *Bulletin of the Seismological Society of America*, 105(2A),
642 622–645. <https://doi.org/10.1785/0120130083>
- 643 Eriş, K. K., Çaçatay, N., Beck, C., Mercier de Lepinay, B., & Corina, C. (2012). Late-
644 Pleistocene to Holocene sedimentary fills of the Çınarcık Basin of the Sea of Marmara.
645 *Sedimentary Geology*, 281, 151–165. <https://doi.org/10.1016/j.sedgeo.2012.09.001>
- 646 Garfield, N., Rago, T. A., Schnebele, K. J., & Collins, C. A. (1994). Evidence of a turbidity
647 current in Monterey Submarine Canyon associated with the 1989 Loma Prieta
648 earthquake. *Continental Shelf Research*, 14(6), 673–686. <https://doi.org/10.1016/0278->
649 [4343\(94\)90112-0](https://doi.org/10.1016/0278-4343(94)90112-0)
- 650 Goldfinger, C., Nelson, C. H., & Johnson, J. E. (2003). Holocene earthquake records from
651 the cascadia subduction zone and northern san andreas fault based on precise dating of
652 offshore turbidites. *Annual Review of Earth and Planetary Sciences*, 31(1), 555–577.
653 <https://doi.org/10.1146/annurev.earth.31.100901.141246>
- 654 Goldfinger, C., Nelson, C. H., Morey, A. E., Johnson, J. E., Patton, J., Karabanov, E.,
655 Gutiérrez-Pastor, J., Eriksson, A. T., Gràcia, E., Dunhill, G., Enkin, R. J., Dallimore, A., &
656 Vallier, T. (2012). Earthquake Hazards of the Pacific Northwest Coastal and Marine
657 Regions Turbidite Event History — Methods and Implications for Holocene



- 658 Paleoseismicity of the Cascadia Subduction Zone Professional Paper 1661 – F. USGS,
659 Professional Paper 1661-F, 170. Retrieved from <http://pubs.usgs.gov/pppp1661f/>
- 660 Grall, C., Henry, P., Tezcan, D., Mercier de Lepinay, B., Becel, A., Geli, L., Rudkiewicz, J.-L.,
661 Zitter, T., & Harnegnies, F. (2012). Heat flow in the Sea of Marmara Central Basin:
662 Possible implications for the tectonic evolution of the North Anatolian fault. *Geology*,
663 40(1), 3–6. <https://doi.org/10.1130/G32192.1>
- 664 Guazzelli, E., Morris, J. F., & Pic, S. (2011). *A Physical Introduction to Suspension*
665 *Dynamics*. Cambridge: Cambridge University Press.
666 <https://doi.org/10.1017/CBO9780511894671>
- 667 Guerrero, M., R  ther, N., & Szupiany, R. N. (2012). Laboratory validation of acoustic Doppler
668 current profiler (ADCP) techniques for suspended sediment investigations. *Flow*
669 *Measurement and Instrumentation*, 23(1), 40–48.
670 <https://doi.org/10.1016/j.flowmeasinst.2011.10.003>
- 671 Guerrero, M., Szupiany, R. N., & Amsler, M. (2011). Comparison of acoustic backscattering
672 techniques for suspended sediments investigation. *Flow Measurement and*
673 *Instrumentation*, 22(5), 392–401. <https://doi.org/10.1016/j.flowmeasinst.2011.06.003>
- 674 Guti  rrez-Pastor, J., Nelson, C. H., Goldfinger, C., & Escutia, C. (2013). Sedimentology of
675 seismo-turbidites off the Cascadia and northern California active tectonic continental
676 margins, northwest Pacific Ocean. *Marine Geology*, 336, 99–119.
677 <https://doi.org/10.1016/j.margeo.2012.11.010>
- 678 H  bert, H., Schindel  , F., Altinok, Y., Alpar, B., & Gazioglu, C. (2005). Tsunami hazard in the
679 Marmara Sea (Turkey): A numerical approach to discuss active faulting and impact on
680 the Istanbul coastal areas. *Marine Geology*, 215, 23–43.
681 <https://doi.org/10.1016/j.margeo.2004.11.006>
- 682 Heezen, B. C., Ericson, D. B., & Ewing, M. (1954). Further evidence for a turbidity current
683 following the 1929 Grand banks earthquake. *Deep Sea Research* (1953), 1(4), 193–202.
684 [https://doi.org/10.1016/0146-6313\(54\)90001-5](https://doi.org/10.1016/0146-6313(54)90001-5)
- 685 Henry, P., A.M.C.   eng  r, M.N.   a  atay (2007) MARNAUT cruise, RV L'Atalante,
686 <https://doi.org/10.17600/7010070>
- 687 Henry, P.,   zeren M.S., Desprez De Gesincourt O., de Saint-Leger E., Libes,, M.,   akir, Z.,
688 Yakupo  lu, N., G  li, L. (2021). EMSO / MAREGAMI Marmara bottom pressure and
689 current records. SEANO. <https://doi.org/10.17882/78928>
- 690 Hsu, S. K., Kuo, J., Lo, C. L., Tsai, C. H., Doo, W. Bin, Ku, C. Y., & Sibuet, J. C. (2008).
691 Turbidity currents, submarine landslides and the 2006 Pingtung earthquake off SW
692 Taiwan. *Terrestrial, Atmospheric and Oceanic Sciences*, 19(6), 767–772.
693 [https://doi.org/10.3319/TAO.2008.19.6.767\(PT\)](https://doi.org/10.3319/TAO.2008.19.6.767(PT))



- 694 Hughes Clarke, J. E. (2016). First wide-angle view of channelized turbidity currents links
695 migrating cyclic steps to flow characteristics. *Nature Communications*, 7(1), 11896.
696 <https://doi.org/10.1038/ncomms11896>
- 697 Ikehara, K., Kanamatsu, T., Nagahashi, Y., Strasser, M., Fink, H., Usami, K., et al. (2016).
698 Documenting large earthquakes similar to the 2011 Tohoku-oki earthquake from
699 sediments deposited in the Japan Trench over the past 1500 years. *Earth and Planetary
700 Science Letters*, 445, 48–56. doi:10.1016/j.epsl.2016.04.009
- 701 Karabulut, H., Güvercin, S. E., Eskikoç, F., Konca, A. Ö., & Ergintav, S. (2021). The
702 moderate size 2019 September Mw5.8 Silivri earthquake unveils the complexity of the
703 Main Marmara Fault shear zone. *Geophysical Journal International*, 224(1), 377–388.
704 <https://doi.org/10.1093/gji/ggaa469>
- 705 Kasaya, T., Mitsuzawa, K., Goto, T., Iwase, R., Sayanagi, K., Araki, E., Asakawa, K., Mikada,
706 H., Watanabe, T., Takahashi, I., & Nagao, T. (2009). Trial of Multidisciplinary
707 Observation at an Expandable Sub-Marine Cabled Station “Off-Hatsushima Island
708 Observatory” in Sagami Bay, Japan. *Sensors*, 9(11), 9241–9254.
709 <https://doi.org/10.3390/s91109241>
- 710 Khripounoff, A., Crassous, P., Lo Bue, N., Dennielou, B., & Silva Jacinto, R. (2012). Different
711 types of sediment gravity flows detected in the Var submarine canyon (northwestern
712 Mediterranean Sea). *Progress in Oceanography*, 106, 138–153.
713 <https://doi.org/10.1016/j.pocean.2012.09.001>
- 714 Le Pichon, X., Chamot-Rooke, N., Rangin, C., & Sengör, A. M. C. (2003). The North
715 Anatolian fault in the Sea of Marmara. *Journal of Geophysical Research*, 108, 2179.
716 <https://doi.org/10.1029/2002JB001862>
- 717 Le Pichon, X., Şengör, A. M. C., Demirbağ, E., Rangin, C., İmren, C., Armijo, R., Görür, N.,
718 Çağatay, N., Mercier de Lepinay, B., Meyer, B., Saatçılar, R., & Tok, B. (2001). The
719 active Main Marmara Fault. *Earth and Planetary Science Letters*, 192(4), 595–616.
720 [https://doi.org/10.1016/S0012-821X\(01\)00449-6](https://doi.org/10.1016/S0012-821X(01)00449-6)
- 721 Liu, J. T., Wang, Y.-H., Yang, R. J., Hsu, R. T., Kao, S.-J., Lin, H.-L., & Kuo, F. H. (2012).
722 Cyclone-induced hyperpycnal turbidity currents in a submarine canyon. *Journal of
723 Geophysical Research: Oceans*, 117(C4), n/a-n/a.
724 <https://doi.org/10.1029/2011JC007630>
- 725 McHugh, C. M. G., Seeber, L., Cormier, M. H., Dutton, J., Cagatay, N., Polonia, A., Ryan, W.
726 B. F., & Gorur, N. (2006). Submarine earthquake geology along the North Anatolia Fault
727 in the Marmara Sea, Turkey: A model for transform basin sedimentation. *Earth and
728 Planetary Science Letters*, 248, 661–684. <https://doi.org/10.1016/j.epsl.2006.05.038>
- 729 McHugh, C. M., Seeber, L., Braudy, N., Cormier, M. H., Davis, M. B., Diebold, J. B.,
730 Dieudonne, N., Douilly, R., Gulick, S. P. S., Hornbach, M. J., Johnson, H. E., Mishkin, K.



- 731 R., Sorlien, C. C., Steckler, M. S., Symithe, S. J., & Templeton, J. (2011). Offshore
732 sedimentary effects of the 12 January 2010 Haiti earthquake. *Geology*, 39(8), 723–726.
733 <https://doi.org/10.1130/G31815.1>
- 734 McHugh, C. M. G., Braudy, N., Çağatay, M. N., Sorlien, C., Cormier, M.-H., Seeber, L., &
735 Henry, P. (2014). Seafloor fault ruptures along the North Anatolia Fault in the Marmara
736 Sea, Turkey: Link with the adjacent basin turbidite record. *Marine Geology*, 353, 65–83.
737 <https://doi.org/10.1016/j.margeo.2014.03.005>
- 738 Mikada, H., Mitsuzawa, K., Matsumoto, H., Watanabe, T., Morita, S., Otsuka, R., Sugioka,
739 H., Baba, T., Araki, E., & Suyehiro, K. (2006). New discoveries in dynamics of an M8
740 earthquake-phenomena and their implications from the 2003 Tokachi-oki earthquake
741 using a long term monitoring cabled observatory. *Tectonophysics*, 426(1–2), 95–105.
742 <https://doi.org/10.1016/j.tecto.2006.02.021>
- 743 Mulder, T., & Cochonnat, P. (1996). Classification of Offshore Mass Movements. *SEPM*
744 *Journal of Sedimentary Research*, Vol. 66. [https://doi.org/10.1306/D42682AC-2B26-](https://doi.org/10.1306/D42682AC-2B26-11D7-8648000102C1865D)
745 [11D7-8648000102C1865D](https://doi.org/10.1306/D42682AC-2B26-11D7-8648000102C1865D)
- 746 Mulder, T., Syvitski, J. P. M., Migeon, S., Faugères, J.-C., & Savoye, B. (2003). Marine
747 hyperpycnal flows: initiation, behavior and related deposits. A review. *Marine and*
748 *Petroleum Geology*, 20(6–8), 861–882. <https://doi.org/10.1016/j.marpetgeo.2003.01.003>
- 749 Nakajima, T., & Kanai, Y. (2000). Sedimentary features of seismoturbidites triggered by the
750 1983 and older historical earthquakes in the eastern margin of the Japan Sea.
751 *Sedimentary Geology*, 135(1–4), 1–19. [https://doi.org/10.1016/S0037-0738\(00\)00059-2](https://doi.org/10.1016/S0037-0738(00)00059-2)
- 752 Normandeau, A., Bourgault, D., Neumeier, U., Lajeunesse, P., St-Onge, G., Gostiaux, L., &
753 Chavanne, C. (2020). Storm-induced turbidity currents on a sediment-starved shelf:
754 Insight from direct monitoring and repeat seabed mapping of upslope migrating
755 bedforms. *Sedimentology*, 67(2), 1045–1068. <https://doi.org/10.1111/sed.12673>
- 756 Okal, E. A., & Synolakis, C. E. (2001). Comment on “Origin of the 17 July 1998 Papua New
757 Guinea Tsunami: Earthquake or Landslide?” by E. L. Geist. *Seismological Research*
758 *Letters*, 72(3), 362–366. <https://doi.org/10.1785/gssrl.72.3.362>
- 759 Özeren, M. S., Çağatay, M. N., Postacioğlu, N., Şengör, a. M. C., Görür, N., & Eriş, K.
760 (2010). Mathematical modelling of a potential tsunami associated with a late glacial
761 submarine landslide in the Sea of Marmara. *Geo-Marine Letters*, 30, 523–539.
762 <https://doi.org/10.1007/s00367-010-0191-1>
- 763 Parker, G. (1982). Conditions for the ignition of catastrophically erosive turbidity currents.
764 *Marine Geology*, 46(3–4), 307–327. [https://doi.org/10.1016/0025-3227\(82\)90086-X](https://doi.org/10.1016/0025-3227(82)90086-X)
- 765 Piper, D. J. W., & Normark, W. R. (2009). Processes That Initiate Turbidity Currents and
766 Their Influence on Turbidites: A Marine Geology Perspective. *Journal of Sedimentary*
767 *Research*, 79(6), 347–362. <https://doi.org/10.2110/jsr.2009.046>



- 768 Piper, D. J. W., Cochonat, P., & Morrison, M. L. (1999). The sequence of events around the
769 epicentre of the 1929 Grand Banks earthquake: initiation of debris flows and turbidity
770 current inferred from sidescan sonar. *Sedimentology*, 46(1), 79–97.
771 <https://doi.org/10.1046/j.1365-3091.1999.00204.x>
- 772 Polonia, A., Vaiani, S. C., & De Lange, G. J. (2016). Did the A.D. 365 Crete
773 earthquake/tsunami trigger synchronous giant turbidity currents in the Mediterranean
774 Sea? *Geology*, 44(3), 191–194. <https://doi.org/10.1130/G37486.1>
- 775 Pope, E. L., Talling, P. J., & Carter, L. (2017). Which earthquakes trigger damaging
776 submarine mass movements: Insights from a global record of submarine cable breaks?
777 *Marine Geology*, 384, 131–146. <https://doi.org/10.1016/j.margeo.2016.01.009>
- 778 Şengör, A. M. C., Grall, C., İmren, C., Le Pichon, X., Görür, N., Henry, P., Karabulut, H., &
779 Siyako, M. (2014). The geometry of the North Anatolian transform fault in the Sea of
780 Marmara and its temporal evolution: implications for the development of intracontinental
781 transform faults. *Canadian Journal of Earth Sciences*, 51(3), 222–242.
782 <https://doi.org/10.1139/cjes-2013-0160>
- 783 Synolakis, C. E., Bardet, J.-P., Borrero, J. C., Davies, H. L., Okal, E. A., Silver, E. A., Sweet,
784 S., & Tappin, D. R. (2002). The slump origin of the 1998 Papua New Guinea Tsunami.
785 *Proceedings of the Royal Society of London. Series A: Mathematical, Physical and*
786 *Engineering Sciences*, 458(2020), 763–789. <https://doi.org/10.1098/rspa.2001.0915>
- 787 Xu, J. P., Noble, M. A., & Rosenfeld, L. K. (2004). In-situ measurements of velocity structure
788 within turbidity currents. *Geophysical Research Letters*, 31(9).
789 <https://doi.org/10.1029/2004GL019718>
- 790 Xu, J. P., Swarzenski, P. W., Noble, M., & Li, A.-C. (2010). Event-driven sediment flux in
791 Hueneme and Mugu submarine canyons, southern California. *Marine Geology*, 269(1–
792 2), 74–88. <https://doi.org/10.1016/j.margeo.2009.12.007>
- 793 Yakupoğlu, N., Uçarkuş, G., Kadir Eriş, K., Henry, P., & Namık Çağatay, M. (2019).
794 Sedimentological and geochemical evidence for seismoturbidite generation in the
795 Kumburgaz Basin, Sea of Marmara: Implications for earthquake recurrence along the
796 Central High Segment of the North Anatolian Fault. *Sedimentary Geology*, 380, 31–44.
797 <https://doi.org/10.1016/j.sedgeo.2018.11.002>
- 798 Zitter, T. A. C., Grall, C., Henry, P., Özeren, M. S., Çağatay, M. N., Şengör, A. M. C.,
799 Gasperini, L., de Lépinay, B. M., & Géli, L. (2012). Distribution, morphology and triggers
800 of submarine mass wasting in the Sea of Marmara. *Marine Geology*, 329–331, 58–74.
801 <https://doi.org/10.1016/j.margeo.2012.09.002>